Supplementary Information (SI) for Lab on a Chip.
This journal is © The Royal Society of Chemistry 2026

Supplementary Information

Intelligent image-activated sorting of large cells enabled by elasto-inertial focusing

Yuzuki Nagasaka,[a] Akihiro Isozaki,[a,b] Hiroki Matsumura,[a,c] Natsumi Tiffany Ishii,[a] Norah Roels,[a] Mina Rassuli,[d] Kelvin C. M. Lee,[a] Walker Peterson,[a] Tianben Ding[a,#] and Keisuke Goda[a,e,f,g,h,i,#]

a. Department of Chemistry, Graduate School of Science, The University of Tokyo, Tokyo 113-0033, Japan.
b. Department of Mechanical Engineering, College of Science and Engineering, Ritsumeikan University, Shiga 525-8577, Japan.
c. Department of Chemical and Biomolecular Engineering, Georgia Institute of Technology, Atlanta, Georgia 30322, USA.
d. Department of Chemistry, RWTH Aachen University, Aachen 52074, Germany.
e. SiRIUS Institute of Medical Research, Tohoku University, Miyagi 980-0872, Japan.
f. Graduate School of Medicine, Tohoku University, Miyagi 980-0872, Japan.
g. International Centre for Synchrotron Radiation Innovation Smart, Tohoku University, Miyagi 980-8577, Japan.
h. Institute of Technological Sciences, Wuhan University, Wuhan, Hubei 430072, China.
i. Department of Bioengineering, University of California, Los Angeles, California 90095, USA.
[#]Corresponding authors: tding@g.ecc.u-tokyo.ac.jp (T.D.); goda@chem.s.u-tokyo.ac.jp (K.G.)

This PDF file includes:

Other supplementary materials for this article:

Data not listed above are available from the corresponding author upon request.

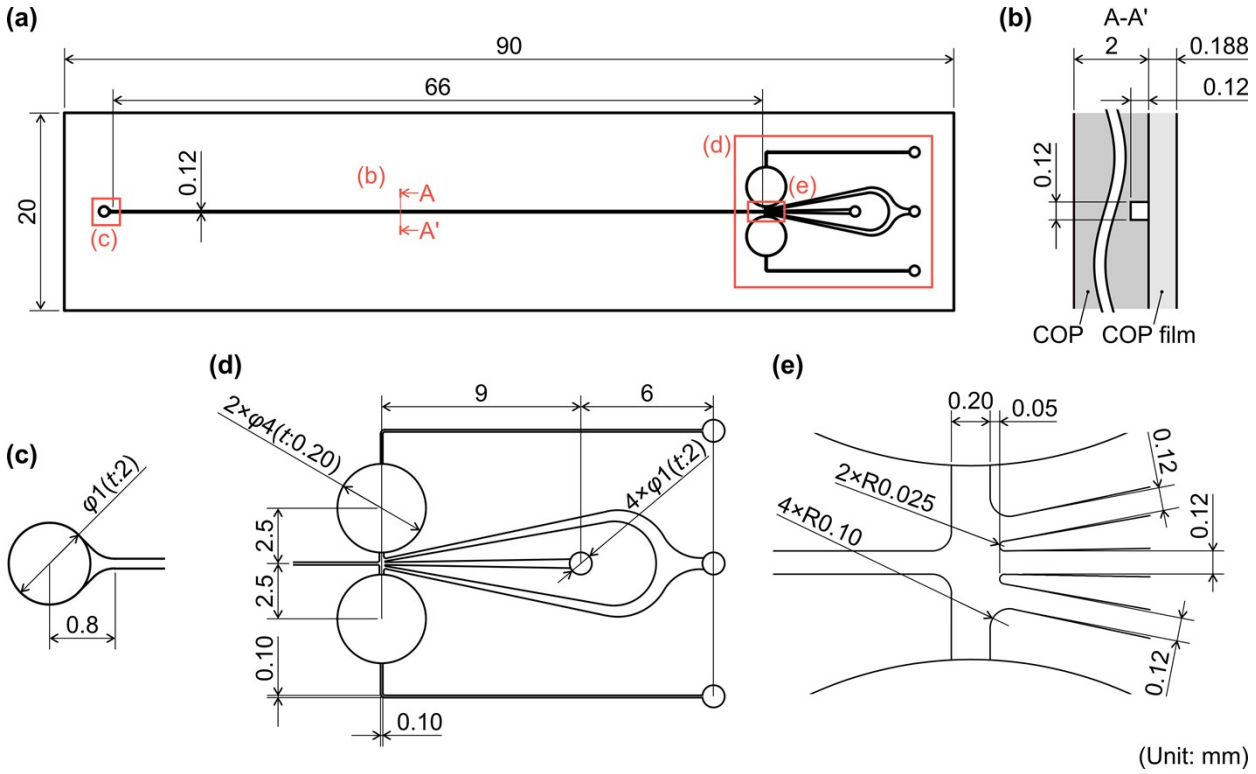

Fig. S1. Dimensions of the microfluidic chip installed in the IACS system. (a) The whole microchannel design. (b) Side view of the microchannel. The cycloolefin polymer (COP)-based microchannel with the side length of 120 μm is sealed by COP film. (c)-(e) Enlarged views of (c) the inlet, (d) the pump wells and outlets, and (e) the sort area. φ, diameter; t: thickness or depth; R, curvature radius.

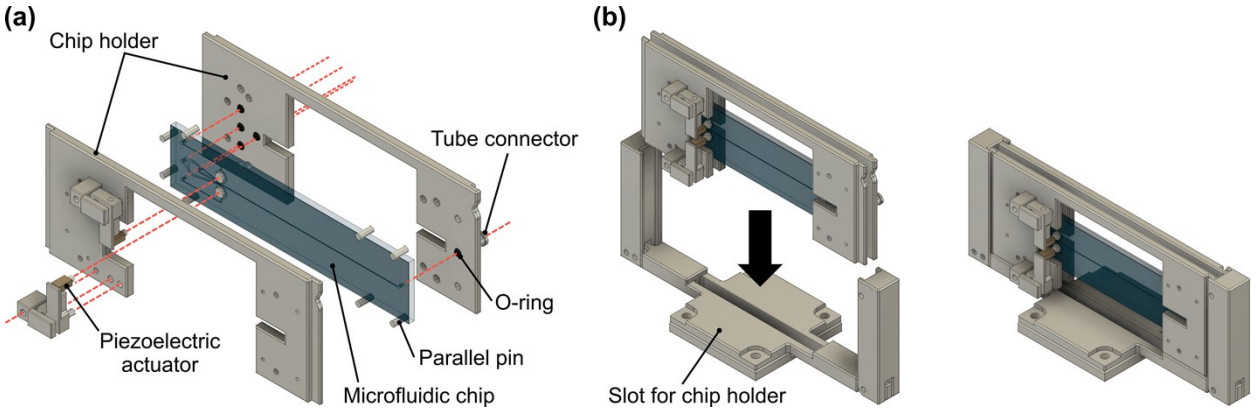

Fig. S2. Integration of the COP-based microfluidic chip into the IACS system. (a) Schematic of the chip holder. The microfluidic chip is sandwiched by the chip holder, connecting to piezoelectric actuators and the flow system via tube connectors. (b) Installation of the chip. The sandwiched chip is set onto the slot in the optical unit of the IACS machine.

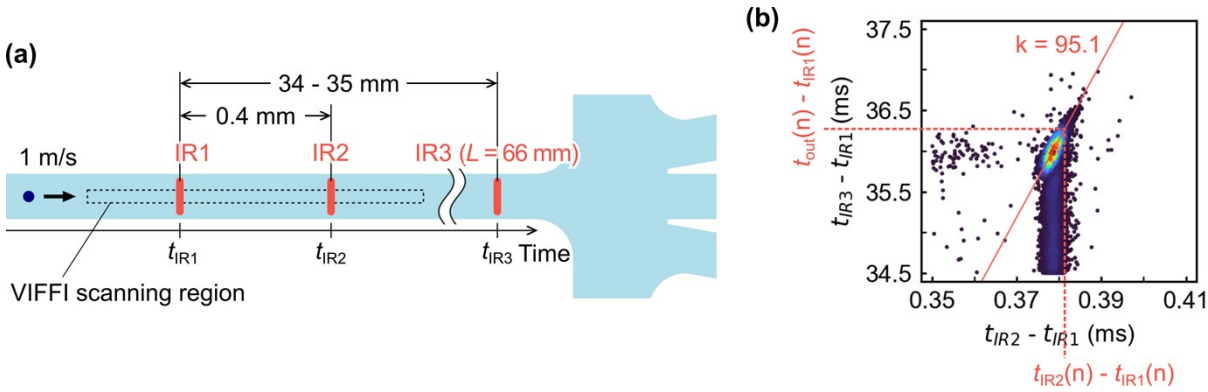

Fig. S3. Measurement of flow speed using infrared (IR) laser. (a) Positions of the IR spots on the microchannel. t_{IR1}, t_{IR2}, and t_{IR3} are the times at which a particle or cell passes IR1, IR2, and IR3, respectively. (b) Kernel density plot of target particles (N = 39,619) with the manually determined linear function (k = 95.1) for sort timing calculation.

5

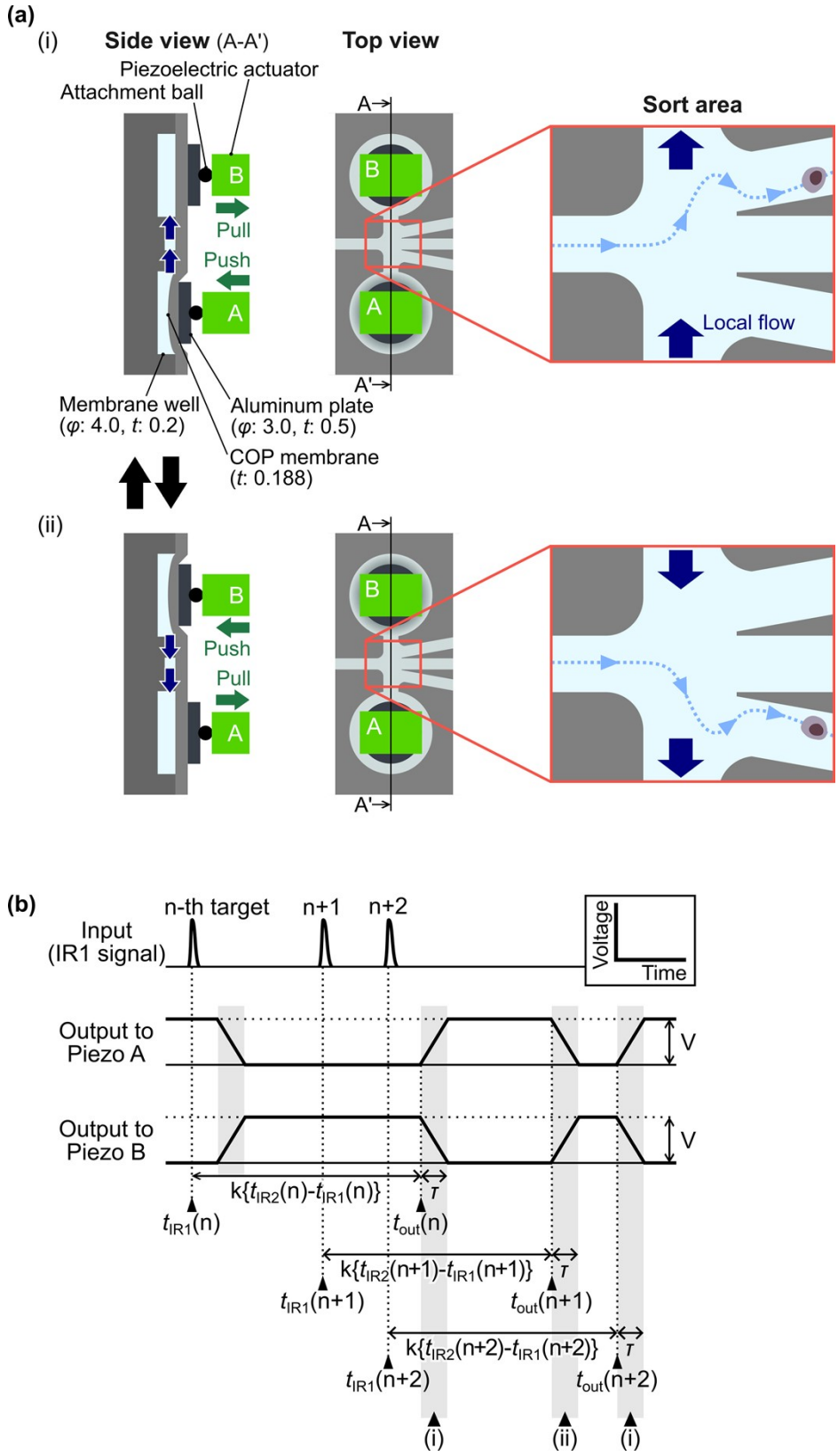

Fig. S4. Sorting actuation by dual-membrane push-pull pumps. (a) Structure and functionality of the membrane pumps. Repeated cycles of (i) up-sort and (ii) down-sort allow rapid and sequential sorting of target particles and cells. φ: diameter. t: thickness or depth. Unit: mm. (b) Input IR1 signals and temporal changes of the applied voltage to the piezoelectric actuators. $t_{IR1}(n)$, $t_{IR2}(n)$, and $t_{IR3}(n)$ are the times when the n-th target particle passes the corresponding IR spots (see Fig. S3). V and τ were set to 40 V and 400 µs, respectively.

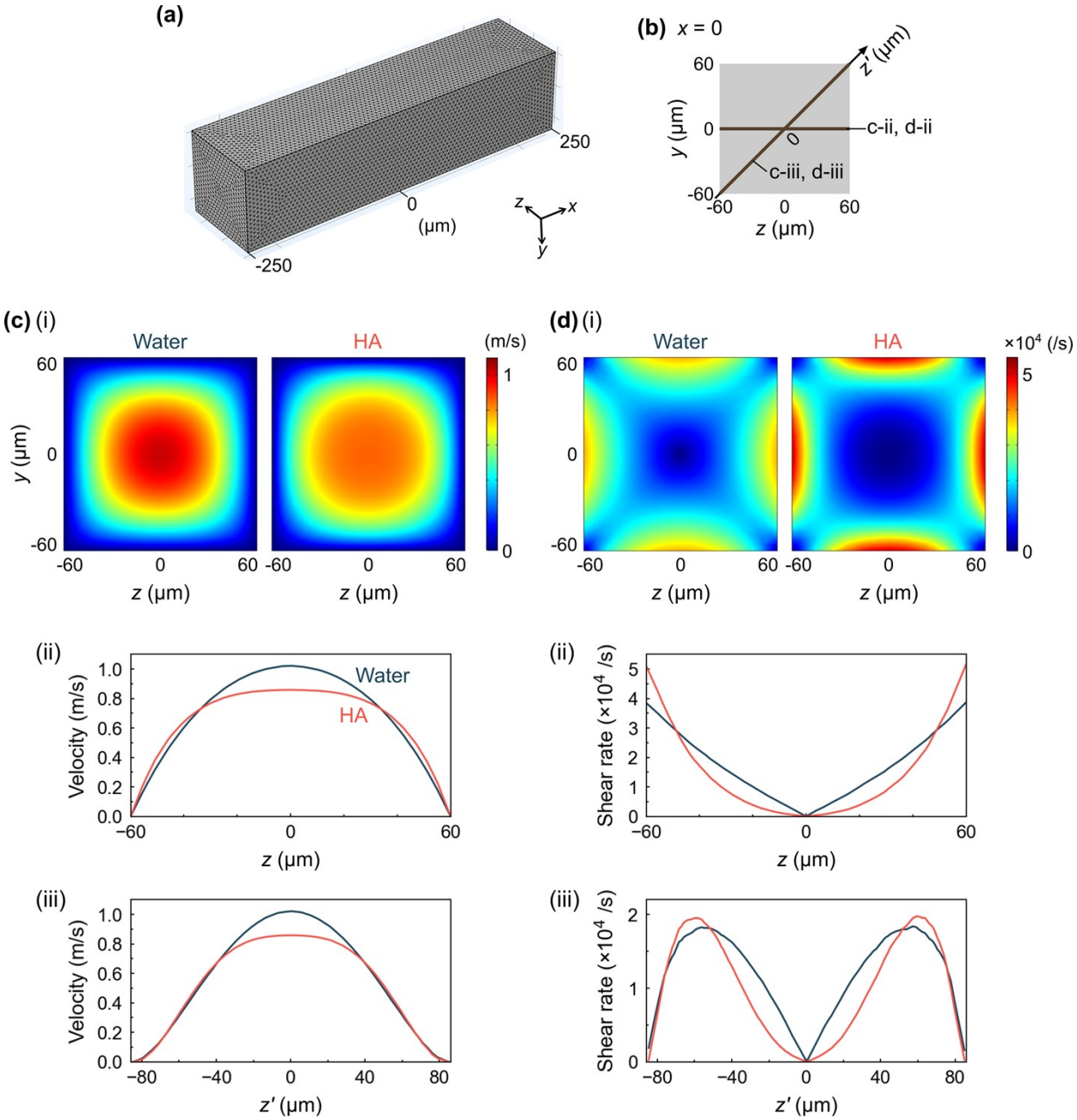

Fig. S5. Computational fluid dynamics simulation of flow of velocity and shear-rate distribution in the elasto-inertial focuser using a finite-element method. (a) Three-dimensional model geometry of the simulated microchannel (length: 500 μm; cross section: 120 μm × 120 μm) and the tetrahedral mesh used for finite-element analysis. (b) Definition of the evaluation planes and lines used for extracting flow velocity and shear-rate profiles, including the mid-plane (x = 0), the horizontal centerline (x = 0, y = 0), and the diagonal line (x = 0, y = z). (c) Simulated flow velocity profiles for water and 0.1% (w/v) HA solution at a volumetric flow rate of 420 μL/min. While water exhibits a parabolic profile with a maximum velocity of ~1.0 m/s at the channel center, the HA solution shows a plug-like velocity profile with a reduced centerline velocity (~0.85 m/s). (d) Corresponding shear-rate profile for water and HA solution under identical flow conditions. In both cases, the shear rate approaches zero near the channel centerline and reaches its maximum near the midpoints of the channel side walls. For the HA solution, the maximum shear rate is on the order of ~5 × 10^4 /s. Particles and cells focused near the centerline therefore experience substantially lower local strain rates than those near the walls.

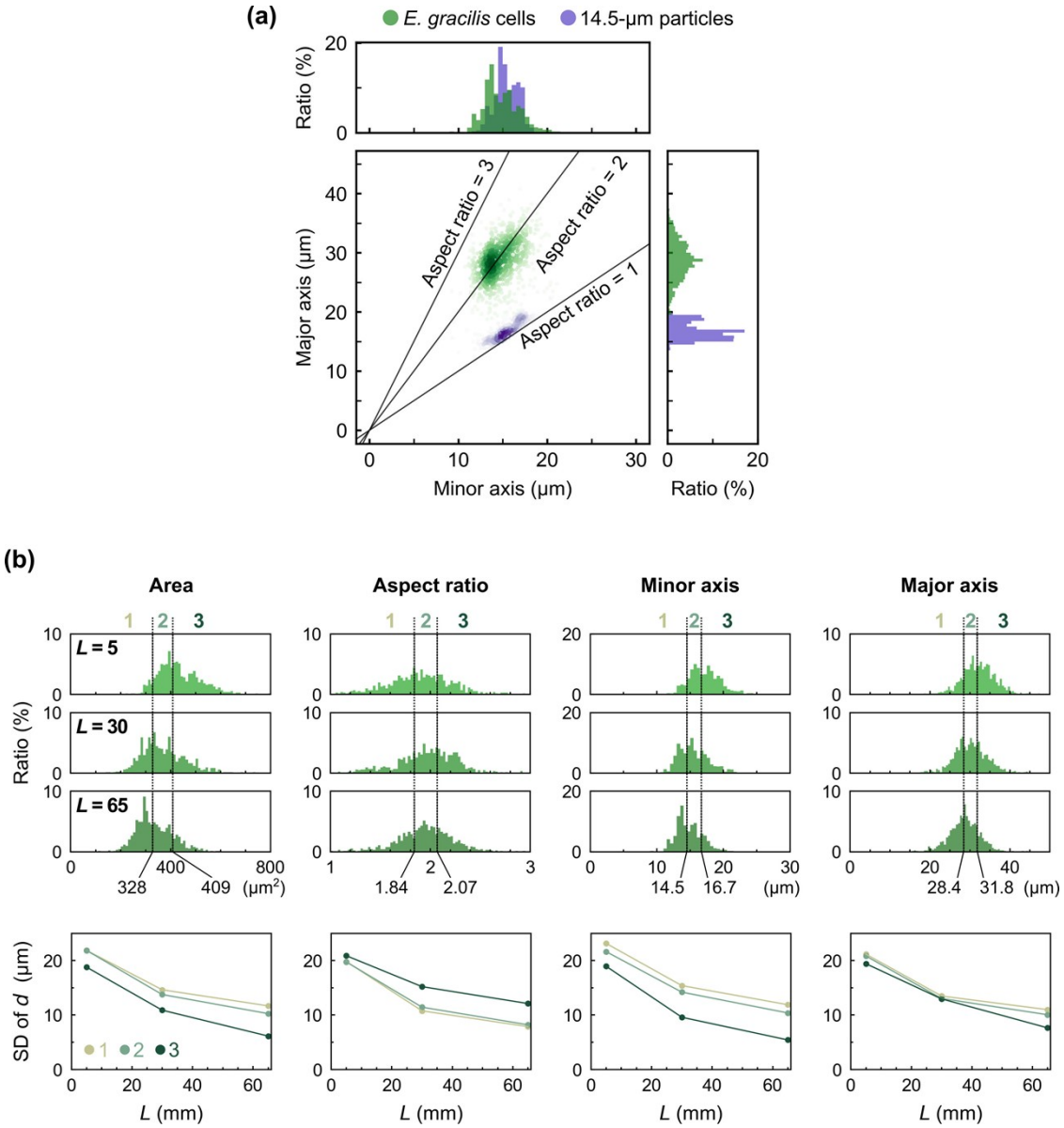

Fig. S6. Effect of shape of *E. gracilis* cells on focusing performance. (a) Scatter plot and histograms of minor and major axes of *E. gracilis* cells and 14.5-μm particles measured from bright-field video frames used for focusing analysis. $N_{E.\ gracilis}$ = 933 and N_{particle} = 983. Aspect ratio = major axis/minor axis. (b) Histograms of *E. gracilis* cell area, aspect ratio, minor axis, and major axis extracted from images acquired at L = 5, 30, and 65 mm. The SD of d (cell displacement) is plotted for cells falling into three ranges corresponding to the lower, middle, and upper one-third of the cell population across all the Ls for each parameter. The plots indicate that small area (< 409 μm^2), large aspect ratio (> 2.07) and short minor axis (< 16.7 μm) are associated with impaired focusing.

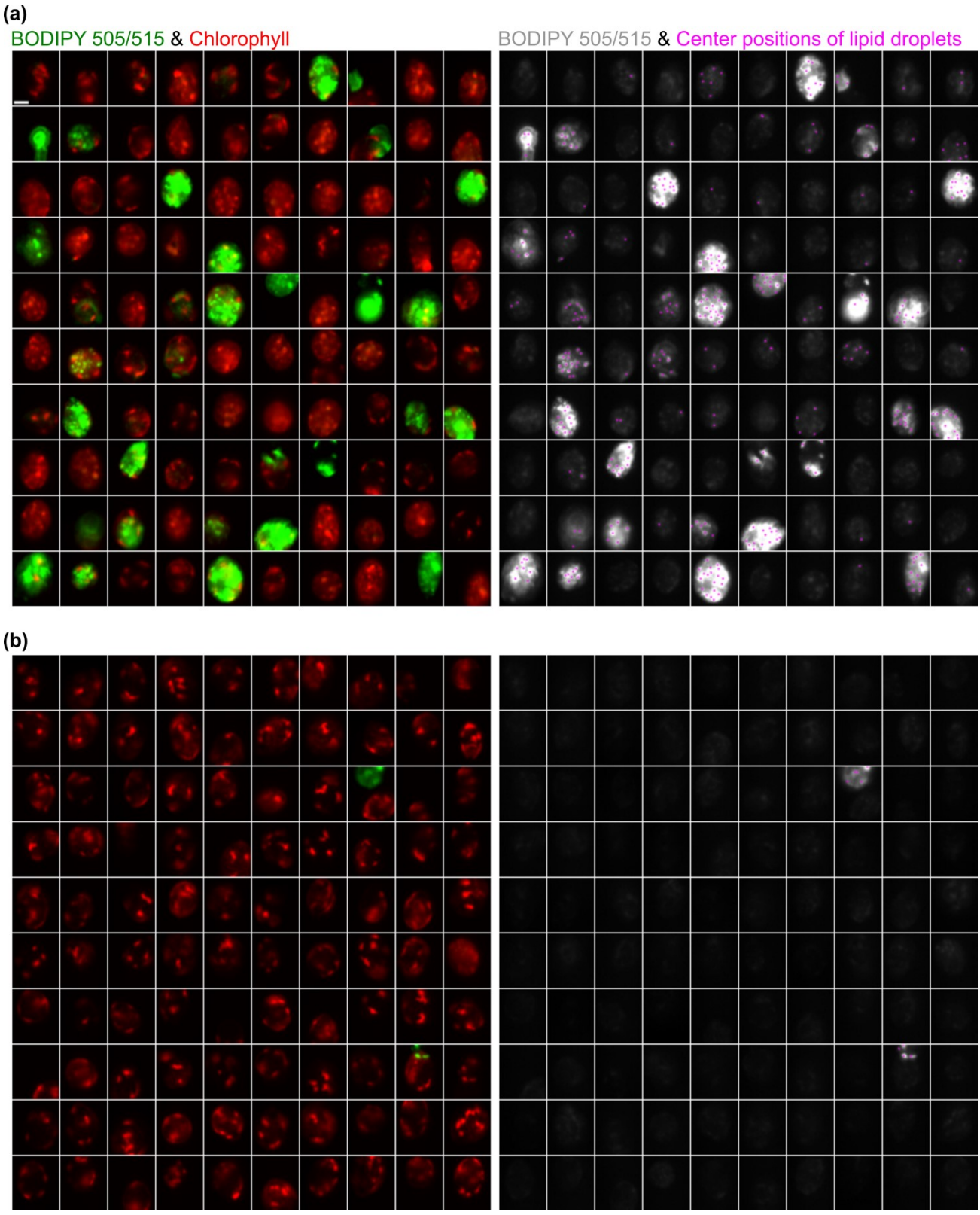

Fig. S7. Images of *E. gracilis* cells acquired during sorting with the 8-layer CNN model. (a) Merged images of cells classified as targets corresponding to those in Fig. 7, showing (left) BODIPY 505/515 fluorescence in green and chlorophyll autofluorescence in red, and (right) BODIPY 505/515 fluorescence in gray with detected lipid droplet center positions used for sorting evaluation after real-time sorting. (b) Corresponding images for cells classified as non-targets. Scale bar, 10 µm.

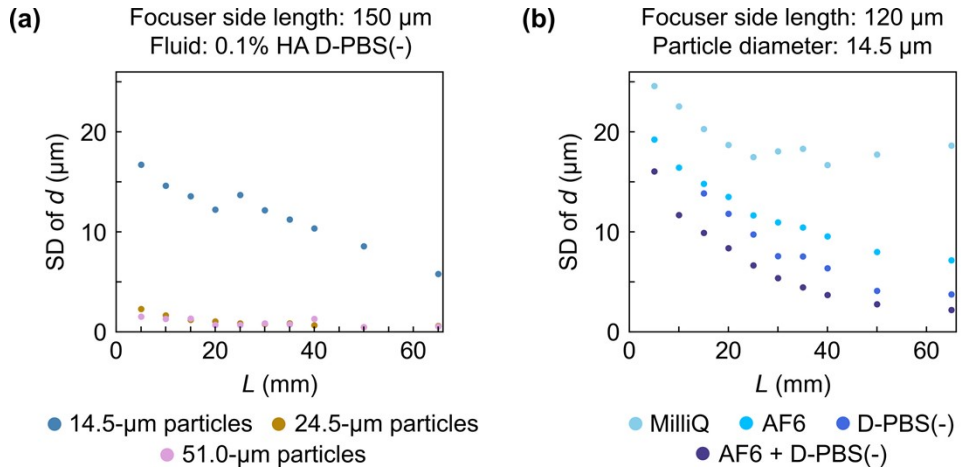

Fig. S8. Elasto-inertial focusing with different focuser side lengths and fluids. (a) Focusing performance in the focuser with a side length of 150 μm. 0.1% sodium hyaluronate (HA) solution in D-PBS(-) was used for the measurement. (b) Focusing performance of 14.5-μm diameter particles using different solvents for the 0.1% HA solution. The focuser side length used here was 120 μm.

Table S1. Rheological parameters of water and 0.1% HA D-PBS(-) solution used in the simulations.

Parameter	Water	0.1% HA*
Density (ρ; kg/m^3)	1000	1000
Zero-shear rate viscosity (μ_0; mPa s)	1	230
Infinite-shear rate viscosity (μ_{inf}; mPa s)	1	0.9
Relaxation time (λ; s)	1	8.7×10^{-4}
Dynamic viscosity ($\mu(\dot{\gamma})$; mPa s)	1	Changes by shear rate ($\dot{\gamma}$) according to Carreau model (n = 0.48)

*Parameters are cited from a previous study (E. J. Lim, *et al.*, *Nat. Commun.*, 2014, **5**, 4120.)

Table S2. Number of particles in each sample measured at different *L* for evaluation of elasto-inertial focusing. Viscoelastic fluid was prepared from the solvents listed and HA powder at 0.1% (w/v).

Fig.	*w* (μm)	Solvent	*φ* (μm)	*L* (mm)									
				5	10	15	20	25	30	35	40	50	65
2	120	D-PBS(-)	10.3	N/A	N/A	918	1013	1051	1048	1151	1051	977	960
			14.5	N/A	N/A	721	635	624	641	636	635	654	650
			24.5	N/A	N/A	679	779	792	757	811	824	845	802
3	120	1:1 of AF-6 & D-PBS(-)	14.5	656	809	991	953	913	958	889	849	945	933
			E. gracilis	703	764	N/A	906	N/A	849	819	976	901	933
S8(a)	150	D-PBS(-)	14.5	951	840	845	898	888	891	828	824	770	853
			24.5	1080	1083	1060	1178	1178	1129	1114	1060	1021	933
			51.0	744	746	714	746	769	671	680	727	751	590
S8(b)	120	MilliQ	14.5	723	1072	959	890	866	1015	974	1041	874	877
		AF-6	14.5	787	1043	974	1087	1095	906	886	1036	1134	1110

Table S3. Composition of AF-6 without nitrogen sources. The omitted nitrogen sources are $NaNO_3$ and NH_4NO_3. They are included in commercially available AF-6 media.
*1: In the case of pH = 6.6.
*2: 140 mg/L of $NaNO_3$ and 22 mg/L of NH_4NO_3 are included in commercially available AF-6.

Compound	Concentration
MES [2-(*N*-morpholino) ethanesulfonic acid]	400 mg/L
Fe(III) citrate nH_2O	2 mg/L
Citric acid	2 mg/L
$MgSO_4 \cdot 7H_2O$	30 mg/L
KH_2PO_4	10 mg/L
K_2HPO_4	5 mg/L
$CaCl_2 \cdot 2H_2O$	10 mg/L
Biotin (Vitamin B7)	2 ng/L
Thiamine HCl (Vitamin B1)	10 ng/L
Pyridoxine (Vitamin B6)	1 ng/L
Cyanocobalamin (Vitamin B12)	1 ng/L
$Na_2EDTA \cdot 2H_2O$	5 mg/L
$FeCl_3 \cdot 6H_2O$	980 µg/L
$MnCl_2 \cdot 4H_2O$	180 µg/L
$ZnSO_4 \cdot 7H_2O$	52 µg/L
$CoCl_2 \cdot 6H_2O$	52 µg/L
$Na_2MoO_4 \cdot 2H_2O$	20 µg/L
NaOH	20 µmol/L*1

Table S4. Comparison of current and our CNN-based IACS systems.

System	Focusing methods	Flow speed (m/s)	Max time between imaging and sorting (ms)	Sorted cells	Cell sorting event rate (eps)
intelligent IACS [a]	Hydrodynamic + acoustic	1	32	Aggregated platelets, *Chlamydomonas reinharditii* (~10 µm diameter)	92.3
intelligent IACS 2.0 [b]	Hydrodynamic	1	32	Yeast (~15 µm length)	1133
User-friendly IACS [c]	Hydrodynamic	0.06-0.07*	3	Leukemia cells (~20 µm diameter)	82.8
Low latency IACS [d]	Hydrodynamic	~0.2	2.3	Leucocytes (~20 µm diameter)	200
COSMOS [e]	Hydrodynamic	~0.2	70	Lung cancer cells (~20 µm diameter)	1
Elasto-inertial intelligent IACS (**this work**)	Elasto-inertial	1	32	*E. gracilis* (~ 20 µm width, ~ 50 µm length)	128

[a] N. Nitta, *et al.*, *Cell*, 2018, **175**, 266-276.; A. Isozaki, *et al.*, *Nat. Protoc.*, 2019, **14**, 2370-2415.
[b] A. Isozaki, *et al.*, *Lab Chip*, 2020, **20**, 2263-2273.
[c] K. Lee, *et al.*, *Lab Chip*, 2021, **21**, 1798-1810.
[d] R. Tang, *et al.*, *Biosens. Bioelecton.*, 2022, **220**, 114865.
[e] M. Salek, *et al.*, *Commun. Biol.*, 2023, **6**, 971.
*Estimation by author from provided volume rate and microchannel cross section.